Crash Sled Testing of Triaxially-Braided CFRP for Improved Vehicular Crashworthiness

Charles R. Ruggeri[1], Rudy T. Haluza[2], J. Michael Pereira, PhD[3], Sandi G. Miller, PhD[4], Charles E. Bakis, PhD[5], and Kevin L. Koudela, PhD[6]

[1]Structural Dynamics Branch, NASA John H. Glenn Research Center, 21000 Brook Park Rd, Cleveland, OH 44135; e-mail: chuck.r.ruggeri@nasa.gov

[2]Department of Engineering Science and Mechanics, Pennsylvania State University, 212 Earth and Engineering Sciences Building, University Park, PA 16802; e-mail: rth5095@psu.edu

[3]Structural Dynamics Branch, NASA John H. Glenn Research Center, 21000 Brook Park Rd, Cleveland, OH 44135; e-mail: mike.pereira@nasa.gov

[4]Ceramic and Polymer Composites Branch, NASA John H. Glenn Research Center, 21000 Brook Park Rd, Cleveland, OH 44135; e-mail: sandi.g.miller@nasa.gov

[5]Department of Engineering Science and Mechanics, Pennsylvania State University, 212 Earth and Engineering Sciences Building, University Park, PA 16802; e-mail: cbakis@psu.edu

[6]Composite Materials Division, Penn State University Applied Research Laboratory, 4000D Applied Sciences Building, University Park, PA 16802; e-mail: klk121@arl.psu.edu

ABSTRACT

The Impact Dynamics Laboratory at NASA Glenn Research Center recently developed a pneumatically-actuated crash sled for investigating the crush behavior of structural elements for vehicular applications. The apparatus includes an adjustable striker mass and specimen support mass, which are mounted on separate rails. This setup provides two advantages over crash sleds with so-called fixed specimen supports: (*i*) it allows for multiple independent measurements of the crush response using different instruments, and (*ii*) the specimen support can be varied and its reaction can be explicitly measured. This paper describes the experimental setup and data analysis methodology and illustrates the capability of the sled for measuring the specific energy absorption (SEA) of triaxially-braided carbon/epoxy composite C-channels and corrugated plates. The corrugated plate had a higher SEA than the C-channel and the SEAs did not vary when the striker mass and velocity were changed so that incident energy was constant.

INTRODUCTION

Fiber-reinforced polymer composite structural elements designed for energy absorption have applications in a number of areas, including the automotive and aerospace industries. Aside from being lightweight and elastically tailorable, thermoset fiber-reinforced polymer composites have more than twice the specific energy absorption (SEA) of aluminum, steel, and structural foam, according to Herrmann et

al. (2002). Furthermore, Farley (1986) found that carbon fiber composites tended to have a higher SEA than glass fiber or aramid fiber composites.

The SEA of composites during crushing impact is typically measured using a drop tower or crash sled with a fixed end (Garner & Adams, 2008). Accelerometer data is used to approximate impact forces and changes in specimen length due to crushing (Garner & Adams, 2008). In other cases, such as Zhou et al. (1991), optical methods and force sensors are used to more directly measure displacement and forces.

Jacob et al. (2001) stated that the impact speed can affect the energy absorption in composite specimens, especially at impact speeds between 7 and 25 m/s. However, others, such as Farley (1991), have shown that the energy absorption capability of some composite laminates, such as $[0/\pm\theta]_2$, are negligibly affected by strain rate.

Farley (1989) demonstrated that the cross-sectional shape of the specimen affects SEA, and Jacob et al. (2002) found that SEA could be doubled by adjusting parameters of the composite specimen structure. Caruthers et al. (1998) pinpointed the cause of the relatively low SEA of square cross sections, compared to circular specimens, to stress concentrations found in the corners of the square. Zhou et al. (1991) showed that a corrugated (sinusoidal)-shaped specimen was more feasible than a round tube in acting as a fastenable structure.

The objectives of the present investigation are two-fold: (*i*) to describe the pneumatically-actuated crash sled recently designed and constructed at the Impact Dynamics Laboratory at NASA Glenn Research Center and (*ii*) to summarize a pilot test program comparing triaxially-braided composite specimens with C-channel and corrugated (trapezoidal) plate geometries at two different impact speeds. The impact speeds were chosen within the range of typical automobile speeds. The crash sled features a movable support mass to which the specimen is attached. Typically, this type of testing is performed on a system where the specimen support is fixed, and the assumption is that the support is rigid. However, energy is clearly transmitted into the support and it is difficult to both quantify and model this energy transmission. In the sled system described in this investigation, the geometry and properties of the support mass are known and can be simply modeled. In addition, the energy transmitted into the support mass is quantified. Accelerometers, force sensors, and high-speed photogrammetry are used to measure the displacement and impact force throughout the impact event. This extensive, redundant suite of instrumentation provides the ability to obtain and compare multiple independent measurements of SEA.

PROCEDURES

Pneumatic Ram Accelerator

A custom-built, pneumatic-actuated crash sled is used for the crush testing of composite specimens. In this device, the test specimen is supported on a heavy stationary mass that is free to move in the direction of impact. The specimen is

impacted by a smaller mass that is accelerated by a pneumatic ram. The rig for crush testing can be discussed in two parts: the accelerator and the sled.

The pneumatic-actuated accelerator is illustrated in Figure 1. A pressure vessel is connected to a smooth bore tube with an inner diameter of 10.16 cm housing a ram intended to accelerate the striker mass of the crash sled. For this study, nitrogen gas was used as the propellant. To accelerate the ram, gas is released from the pressure vessel using a Mylar burst disk, which consists of two Mylar sheets with a Nichrome wire embedded between them.
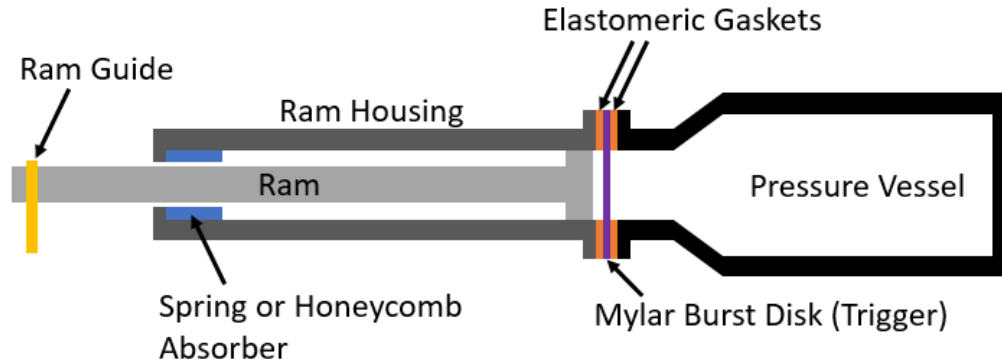
(a)
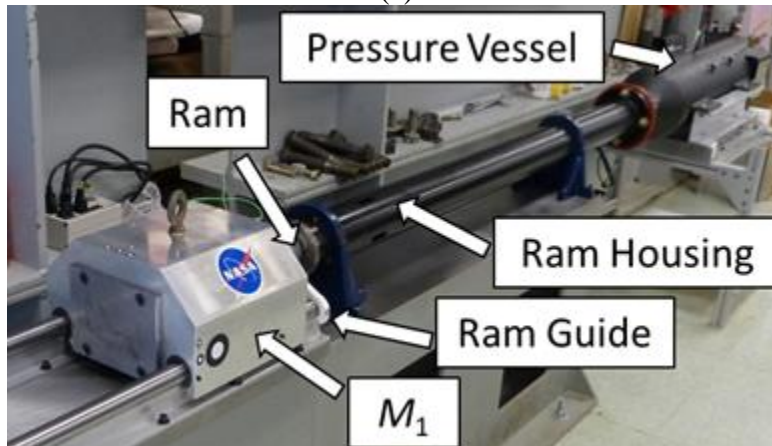
(b)

Figure 1. (a) Illustration of cross-sectional view of pneumatic ram accelerator (not to-scale; colors chosen for clarity). (b) Photo of ram accelerator and M_1.

Once the pressure vessel is filled to its desired pressure, a current is passed through the Nichrome wire that melts the Mylar and allows the nitrogen to escape from the pressure vessel. Subsequently, the ram is accelerated through the housing until a flange welded to the back of the ram contacts a spring or honeycomb energy- absorbing structure held in place by the end of the ram housing. A spring is used to stop the ram at impact velocities up to 15 m/s; at higher velocities, an aluminum honeycomb annulus is used. The ram is supported by a guide that attaches to the rails of the striker mass. The footprint of the test apparatus is approximately 5.5 m in length and 0.5 m in width. Different impact masses can be used. Currently, the masses range from approximately

9 to 145 kg. The length of the ram housing is 2 m, which governs the distance over which the impacting mass is accelerated. The limits of the impact energy have not been determined, but it is estimated that an impact energy of 5 kJ can be achieved. Constraints on the current geometry of the apparatus limit the test specimen size to approximately 15 cm laterally and 25 cm lengthwise.

Sled Section

The striker mass (M_1), support mass (M_2), specimen, specimen plate (M_{PL}), bearings, and rails are hereafter referred to as the sled section, which is illustrated in Figure 2.
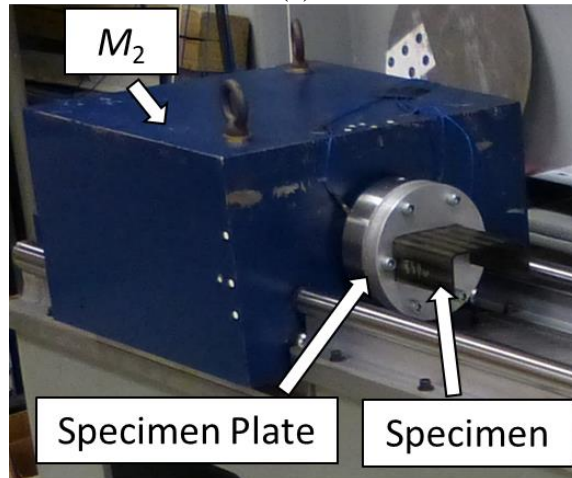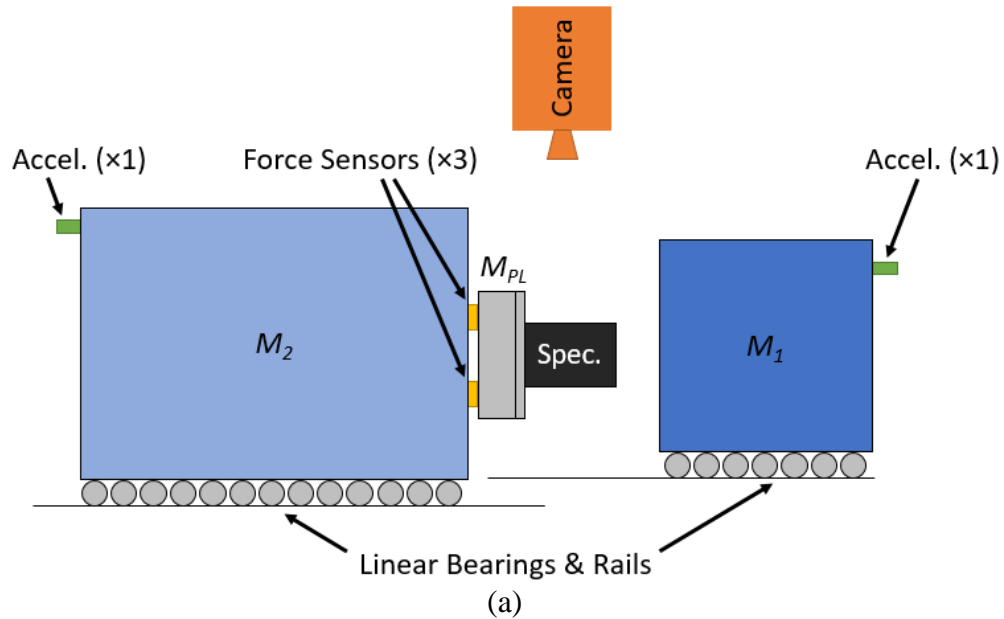

(a)

(b)

Figure 2. (a) Illustration of sled section with labeled masses (M_1, M_2, and M_{PL}), specimen (Spec.), accelerometers (Accel.), force sensors, and camera. M_1 and M_2 traverse on separate bearings and rails. Not to-scale; transducers enlarged and colorized for clarity. (b) Photograph of support mass (M_2), specimen plate, and specimen.

M_1 and M_2 each have four linear bearings supported on their individual set of rails. The rails were leveled and aligned during construction of the sled section. A shock absorber behind M_2 keeps the mass from running off the end of its track, which subsequently keeps M_1 on its track. The specimen is held in place by a two-part fixture (referred to as the specimen plate) attached to M_2 via six bolts.

The specimen plate includes a thin plate in front with a cut-out corresponding to the cross-section of the specimen profile and a thick plate in back, against which the specimen bears during a test. Prior to each test, a specimen is pushed through the cut-out in the thinner plate until flush with the thicker plate and adhered in place with a two-part epoxy.

The sled section is equipped with several transducers as well as high-speed cameras to record the impact event and allow photogrammetric measurements. Each mass has its own accelerometer to record accelerations. Three piezoelectric force sensors are placed between the specimen plate and M_2 to measure the reaction force between the specimen plate and M_2. The top-view high-speed camera is used to track the displacement of both masses during the impact event. Velocity can be calculated using photogrammetry by numerically differentiating the displacement measurements with respect to time. More information regarding the transducers and high-speed camera is shown in Table 1.

Table 1. Instrumentation for Data Acquisition.

Equipment	Make & Model	Record Rate	Range
Force Sensor (×3)	PCB[a] 203B/FCS-5	1.25 MHz	89 kN
M_1 Accelerometer	PCB[a] ICP 350C04	1.25 MHz	5000 g
M_2 Accelerometer	PCB[a] ICP 353B14	1.25 MHz	1000 g
High-speed Camera	Photron[b] Fastcam SA-Z	70000 fps	N/A

[a]PCB Piezotronics (Depew, New York)
[b]Photron (Tokyo, Japan)

Normal operation of the system is as follows. Initially, M_1 is in contact with the end of the ram. M_1 is accelerated by the ram down the rails until the ram is stopped by the energy absorber within the ram housing. At this point, directly before impacting the specimen, the ram and M_1 separate. While M_1 travels unassisted by the ram, a laser-based proximity trigger is activated, which initiates the data acquisition of the transducers and high-speed camera.

Impact Event

Figure 3 illustrates the impact event, which is defined as the time between first contact of M_1 and the specimen and the separation of M_1 and the specimen. The moment just before impact is considered to be time $t = 0$, when the specimen plate and the support mass (collectively referred to as M_{PL}/M_2) have zero initial velocity ($V_{2i} = 0$) and M_1 is about to make first contact with the specimen with a non-zero initial impact velocity ($V_{1i} > 0$). This point in time is the reference for displacement.

Thus, δ_1 and δ_2 represent the change in distance of M_1 and M_2, respectively, relative to their position at $t = 0$. V_1 and V_2 are herein used to represent the velocities of M_1 and M_{PL}/M_2, respectively, at any time during the impact event.
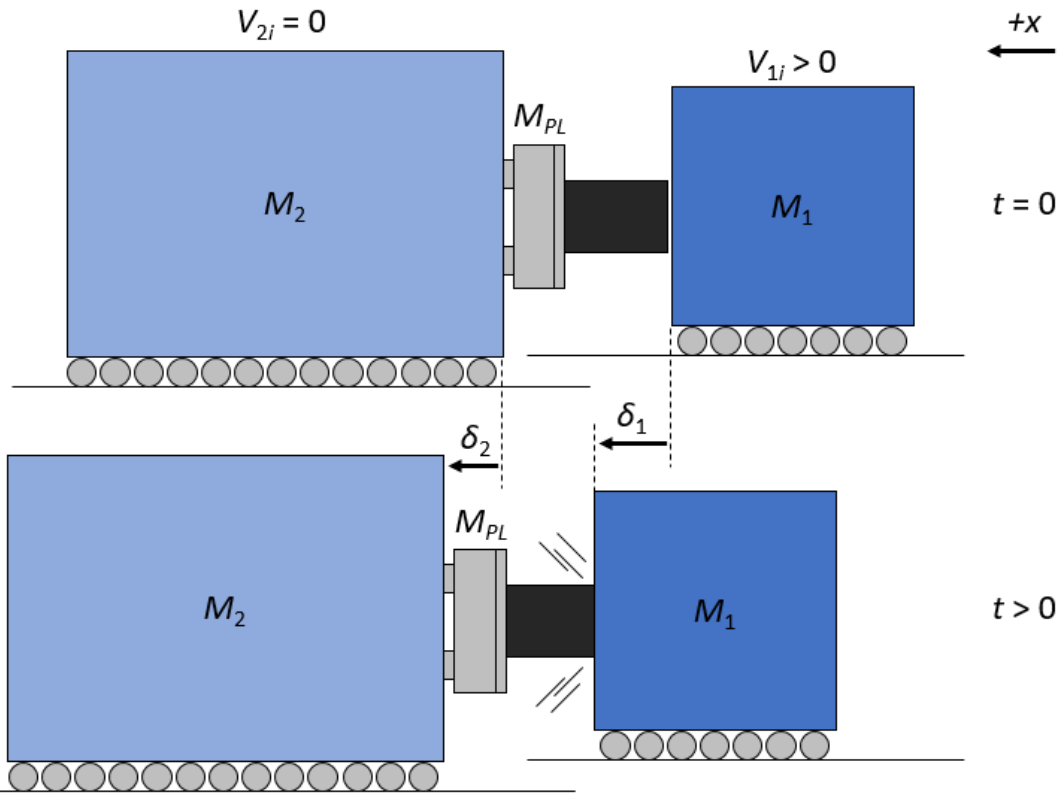

Figure 3. Illustration of sled section at the instant before ($t = 0$) and after ($t > 0$) impact.

Mechanics of Impact

Measurement of SEA is typically the primary objective of these testing programs. Energy absorption is calculated using four methods. The first three methods involve the work-energy principle, which states that the change in kinetic energy (ΔKE) of a body is equal to work (W) done on the body. By neglecting friction, there are no external forces acting on the sled section once the ram separates from M_1. Although there is inherently friction in the system, both masses are supported by bearings and the frictional forces are low (on the order of 5 N) compared to the impact forces, which are typically tens of thousands of Newtons. Thus, the energy absorbed by the specimen is assumed to be equal to the sum of the change in kinetic energy of M_1 and M_{PL}/M_2. As shown in the free body diagrams in Figure 4, work is only done by the impact force (F_{imp}) on each mass.
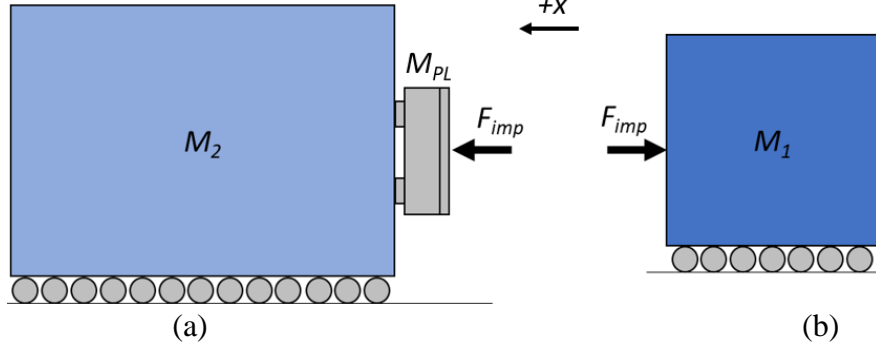
Figure 4. Free body diagrams of (a) M_{PL}/M_2 and (b) M_1 (neglecting friction).

By Newton's third law, the impact force on M_1 and M_{PL}/M_2 is equal and opposite. The specimen mass is neglected because it is several orders of magnitude lower than the mass of M_1 and M_{PL}/M_2.

The ΔKE of the two masses over any time step during the impact event can be calculated by summing W_2 (the work done to M_{PL}/M_2) and W_1 (the work done to M_1) using Eqn. 1 where $\bar{F}_{imp}$ represents the average F_{imp} over a given time step and $\Delta\delta$ is the change in displacement of either mass over that time step.

$$\Delta KE = W_2 + W_1 = \bar{F}_{imp}\Delta\delta_2 - \bar{F}_{imp}\Delta\delta_1 \tag{1}$$

While the specimen is being crushed, $\Delta\delta_2 < \Delta\delta_1$. The work done to the specimen, W_{SP}, is defined as the negative of $W_2 + W_1$. Because the crush displacement, δ_{crush} (i.e. the change in length of the specimen due to crushing or $\delta_1 - \delta_2$), is a value of interest, it is helpful to format the equations for work using the change in δ_{crush} over a time step, $\Delta\delta_{crush}$.

$$W_{SP} = -(W_2 + W_1) = \bar{F}_{imp}(\Delta\delta_1 - \Delta\delta_2) = \bar{F}_{imp}\Delta\delta_{crush} \tag{2}$$

A numerical integration scheme is implemented for Eqn. 2 to determine the work done between the jth and $(j+1)^{th}$ time step ($j = 0, 1, 2...$), as shown in Eqn. 3 and Figure 5a.

$$W_{SP_{j+1}} = \frac{F_{imp_{j+1}} + F_{imp_j}}{2}\left(\delta_{crush_{j+1}} - \delta_{crush_j}\right) \tag{3}$$

Assuming that M_2 and the M_{PL} act as a rigid body and that the mass of the specimen is negligible, the force of the impact at the jth time step can be calculated using the acceleration of M_{PL}/M_2, a_2, or the acceleration of M_1, a_1, as shown in Eqn. 4.

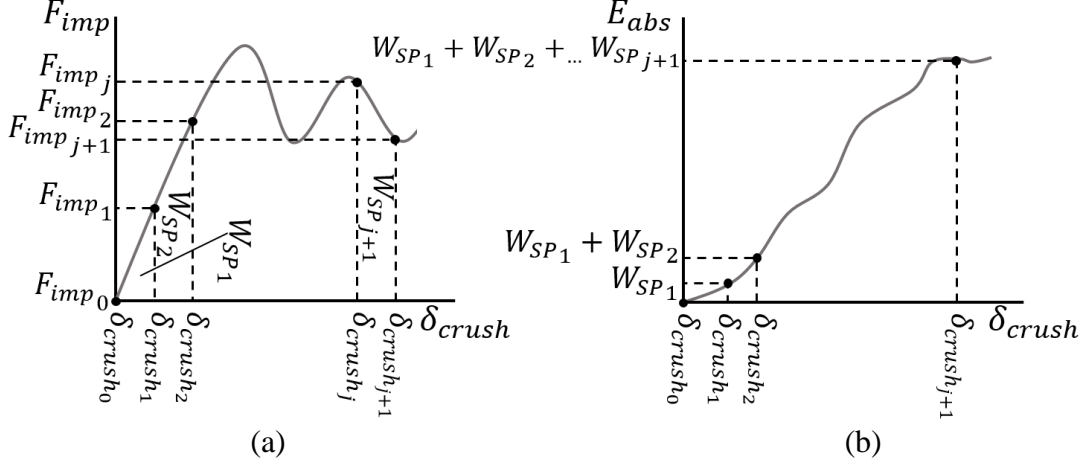$$F_{imp_j} = (M_2 + M_{PL})a_{2_j} = M_1 a_{1_j} \tag{4}$$

Figure 5. Visual representations of the calculation for (a) W_{SP} and (b) E_{abs} from Eqns. 3 and 9, respectively.

An alternative approach can be used to calculate work based on the data from the force sensors located between M_{PL} and M_2. However, as shown in Figure 6, the force sensors measure an internal force, F_{FS}, that is not equal to F_{imp} because of the mass of the specimen plate. If we consider M_{PL} and M_2 separately, Newton's second law for M_2 at the jth time step can be written as Eqn. 5.

$$F_{FS_j} = M_2 a_{2_j} \tag{5}$$

Similarly, Newton's second law for the specimen plate can be written as Eqn. 6, assuming the specimen plate and M_2 accelerate at the same rate.

$$F_{imp_j} - F_{FS_j} = M_{PL} a_{2_j} \tag{6}$$

Solving Eqn. 5 in terms of a_2 and substituting this value into Eqn. 6 yields Eqn. 7.

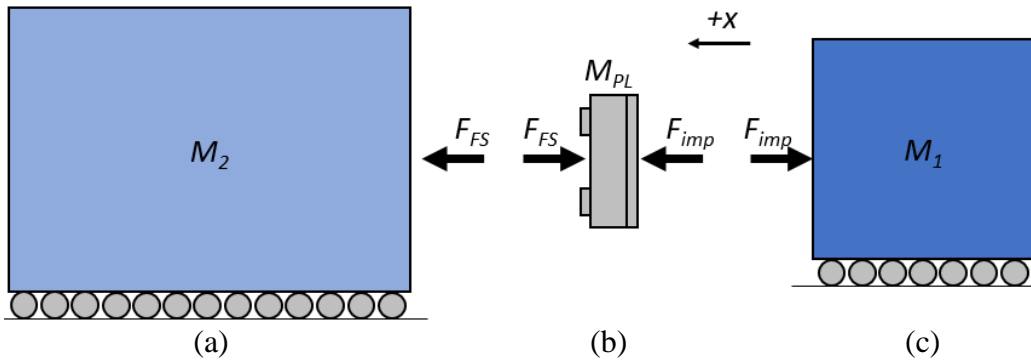$$F_{imp_j} - F_{FS_j} = M_{PL} \left(\frac{F_{FS_j}}{M_2} \right) \tag{7}$$

Figure 6. Free body diagrams of (a) M_2, (b) the specimen plate (M_{PL}), and (c) M_1 (neglecting friction). M_2 and M_{PL} separated to show internal forces.

Simplifying Eqn. 7 leads to Eqn. 8, which relates F_{imp} to F_{FS} at the jth time step.

$$F_{imp_j} = M_{PL}\left(\frac{F_{FS_j}}{M_2}\right) + F_{FS_j} = \left(\frac{M_{PL}}{M_2} + 1\right)F_{FS_j} \tag{8}$$

To calculate the cumulative energy absorbed up to the $(j+1)$th time step during the impact event, E_{abs}, the incremental energy in each step is summed over the $j+1$ intervals of time as shown in Eqn. 9.

$$E_{abs_{j+1}} = \sum_{m=1}^{j+1} W_{SP\,m} \tag{9}$$

Figure 5b shows a visual representation of Eqn. 9. The value for E_{abs} can also be obtained directly using velocity measurements derived from the photogrammetry displacement data. This is shown in Eqn. 10 by subtracting the initial kinetic energy of the masses from the current kinetic energy of the masses at the jth time step and changing the sign to ensure that E_{abs} is positive.

$$E_{abs_j} = -\left\{\left[\frac{1}{2}M_1V_1^2 + \frac{1}{2}(M_2 + M_{PL})V_2^2\right]_j - \left(\frac{1}{2}M_1V_{1i}^2\right)\right\} \tag{10}$$

Unlike Eqn. 9, the method shown in Eqn. 10 does not rely on a summation because the change in kinetic energy can be calculated by direct comparison to the original energy of the sled section at $t = 0$ when only M_1 has kinetic energy. Equation 10 assumes that M_{PL} and M_2 act as a rigid body.

Data Processing

For this investigation, the maximum E_{abs} value in each dataset was used in the calculation for SEA. Prior to testing, the length, L_{SP}, and mass, m_{SP}, of each specimen was recorded. The mass per unit length of the specimen, ρ_L, was calculated by dividing the mass of the specimen by the total length.

$$\rho_L = \frac{m_{SP}}{L_{SP}} \tag{11}$$

SEA was calculated by dividing the maximum-measured E_{abs} by the mass of the specimen that is crushed, or ρ_L multiplied by δ_{crush}.

$$SEA = \frac{(E_{abs})_{max}}{(\rho_L)(\delta_{crush})} \tag{12}$$

A photogrammetry software, TEMA (Image Systems Motion Analysis, Linköping, Sweden), was used to measure δ_{crush}. While δ_{crush} can be calculated from the accelerometer data, direct measurement avoids issues associated with integrating

signals that may have small non-zero offsets. The δ_{crush} data were filtered using a SAEJ CFC 120 filter (SAE International, Warrendale, PA), which is comparable to a low-pass digital filter with a 200 Hz cutoff, to remove noise from mechanical vibrations in M_1 and M_2. Since the photogrammetry data and the data from the transducers were recorded at different rates, the filtered δ_{crush} values were linearly interpolated between measurements to obtain values for δ_{crush} at times corresponding to the transducer measurements recorded every 0.8 μs. This allowed the transformation of the transducer data to the displacement domain. The beginning and end of the impact event were manually selected using the force sensor data and uniformly used in all data sets for a given specimen. Due to the way in which SEA is computed, filtering the force and accelerometer data had little effect on the calculated SEA; the unfiltered data and filtered data produced approximately the same SEA, and the SEA calculated using unfiltered data was selected to be reported.

C-Channel & Corrugated Specimen Manufacturing

The prepreg material used in this study was fabricated from triaxially-braided T700S carbon fiber (Toray, Decatur, AL) and TC275-1 toughened epoxy resin (Tencate, Morgan Hill, CA). The prepreg, with a fiber areal weight of 536 gsm and a 38% resin content, was procured from Tencate. The dry carbon fiber braid was manufactured by A&P Technologies (Summerside, OH) and consisted of a quasi-isotropic [0/±60] braid (QISO H-59) with 24K tows in the axial direction (0° tows) and 12K tows in the bias directions (±60° tows). The fiber areal weight was equal in each tow direction, which produces a nominally quasi-isotropic laminate.

Aluminum tools were used to provide the required laminate shapes. As shown in Figure 7, the C-channel specimen had an open rectangular profile with different radii defined for the two corners and the corrugated specimen consisted of a trapezoidal profile with rounded corners. Figure 8 shows the laminates being vacuum bagged against a single aluminum tool. The laminates were autoclave cured following the vendor recommended cure process: 1) apply full vacuum with an external pressure of 103 kPa, 2) heat to 107°C at a rate of 2.25°C per minute, 3) increase pressure to 586 kPa and hold for 60 minutes, 4) heat to 177°C at a rate of 2.25°C per minute, 5) release vacuum, hold for 120 minutes, and cool to 21°C at a rate of 1.1°C per minute. Both channels were fabricated with six layers of the [0/±60] braid, with the 0-deg. tows all aligned in the axial (crush) direction of the channels. The average thickness of the cured laminates was 3.43 mm. The fiber areal weight, cured ply thickness of the prepreg, and a fiber density of 1.8 g/cc yield an approximate fiber volume fraction of 0.52.

After debagging, laminates were cut in half and the two resulting specimens were trimmed to a length of 120 mm. A steeple trigger was manufactured into the front edge of each specimen using a CNC machine. The steeple trigger, as shown in Figure 9, was formed by removing material at a 45° angle relative to the length of the specimen. This pointed edge promotes a crushing failure mode upon impact.
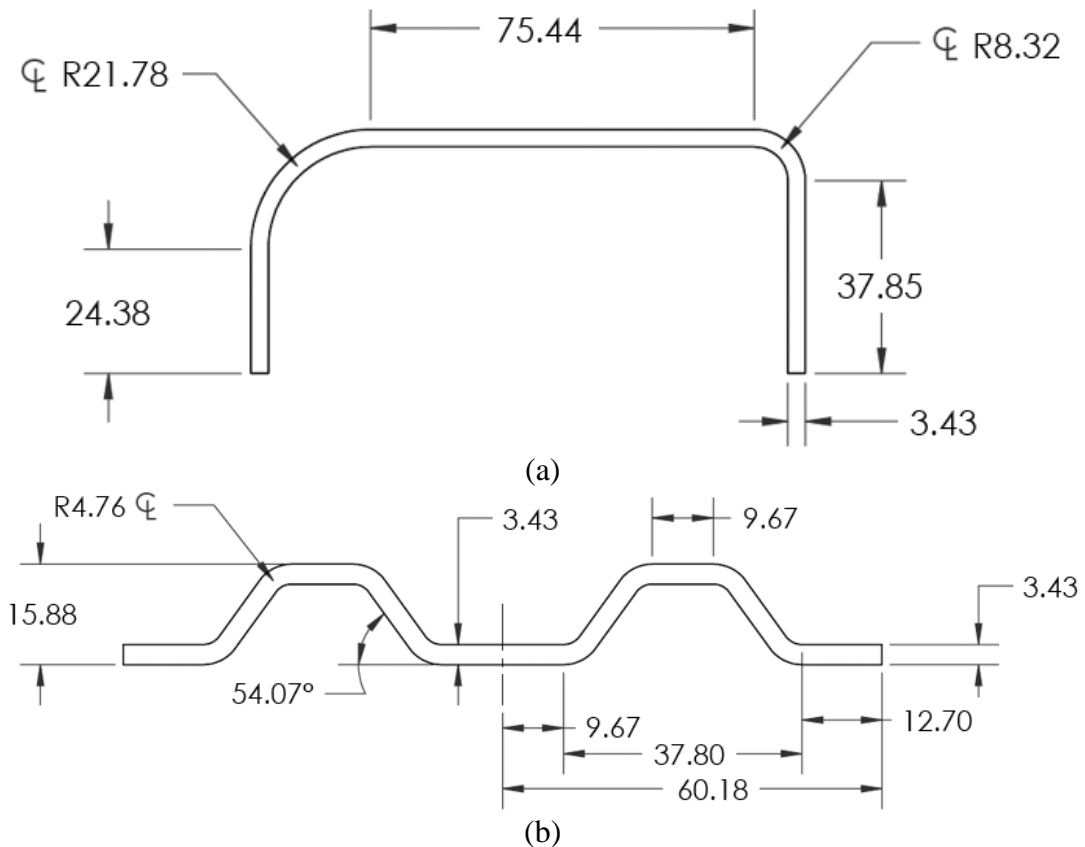
Figure 7. Specimen cross sections for the (a) C-channel and (b) corrugated geometries. Dimensions in mm.
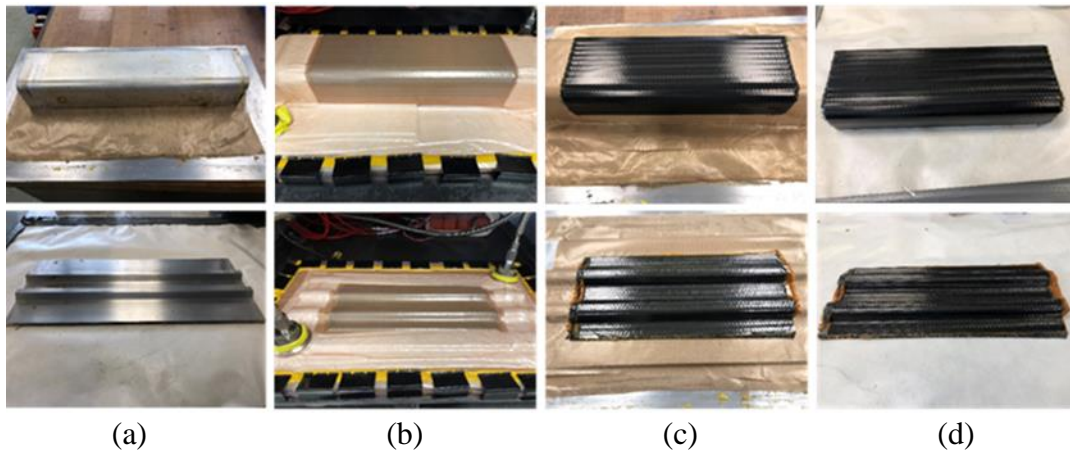

Figure 8. C-channel (top row) and corrugated (bottom row) specimens at various steps in manufacturing: (a) prepared tool, (b) vacuum bagged before autoclave cure, (c) debagged on tool after cure, and (d) cured part.
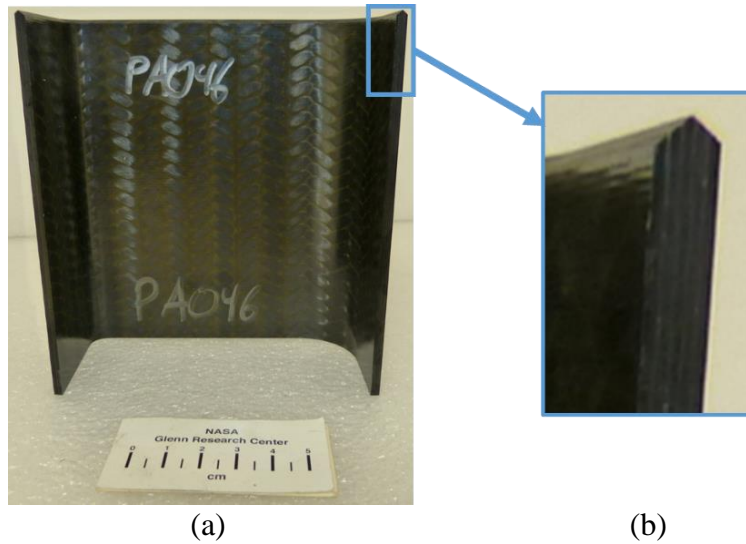
Figure 9. C-channel specimen (a) with magnified steeple trigger (b). Axial (0-deg.) tows of the braided preform are vertical in (a) and (b).

Test Plan

Table 2 shows the test plan used for the crush testing of the C-channel and corrugated specimens. The tests were conducted at two different velocities, 11.2 m/s (25 mph) and 22.4 m/s (50 mph), resulting in approximately equal impact kinetic energies of 2160 and 2350 J, respectively, based on the available striker masses (M_1). For both conditions the mass of M_2 was 315.4 kg.

Table 2. Test plan for C-channel and corrugated specimens.

Test Condition	Specimen Geometry	
	C-Channel	Corrugated
$M_1 = 34.47$ kg $V_1 = 11.2$ m/s (25 mph)	8 specimens	9 specimens
$M_1 = 9.36$ kg $V_1 = 22.4$ m/s (50 mph)	5 specimens	5 specimens

RESULTS

The corrugated and C-channel specimens exhibited different modes of failure (Figure 10). The geometry of the corrugated specimens appeared to limit the widespread delamination and generally failed in a crushing and tearing mode. The C-channel specimens exhibited widespread delamination with some crushing and tearing at the radii. Figure 11 shows the summary of SEA results for the two specimen geometries tested at the different impacting velocities. For this series of tests, the M_2 accelerometer measured values exceeding its maximum, due to noise, which caused errors in data processing; thus, these values were not included in the data analysis. However, the SEA measurements from the accelerometer on M_1, the force sensors, and photogrammetry were in agreement with each other, as shown by overlapping standard deviations. The source of the noise in the M_2 accelerometer is being investigated and addressed.

The crush testing results showed that the corrugated specimens had nearly twice the SEA of the C-channel specimens. The lower SEA in the C-channel specimens may be due to the greater extent of delamination in the C-channel specimens compared to the corrugated specimens as shown in Figure 10. Additionally, the change in impact velocity (while keeping kinetic energy approximately constant by altering M_1) had a negligible effect on SEA for both specimen geometries.
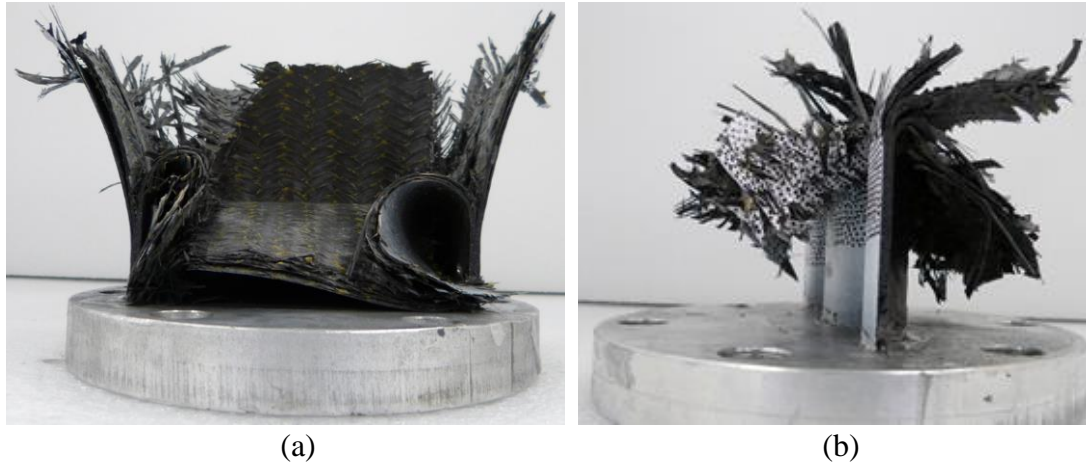

(a)   (b)

Figure 10. Crushed C-channel (a) and corrugated (b) specimens.
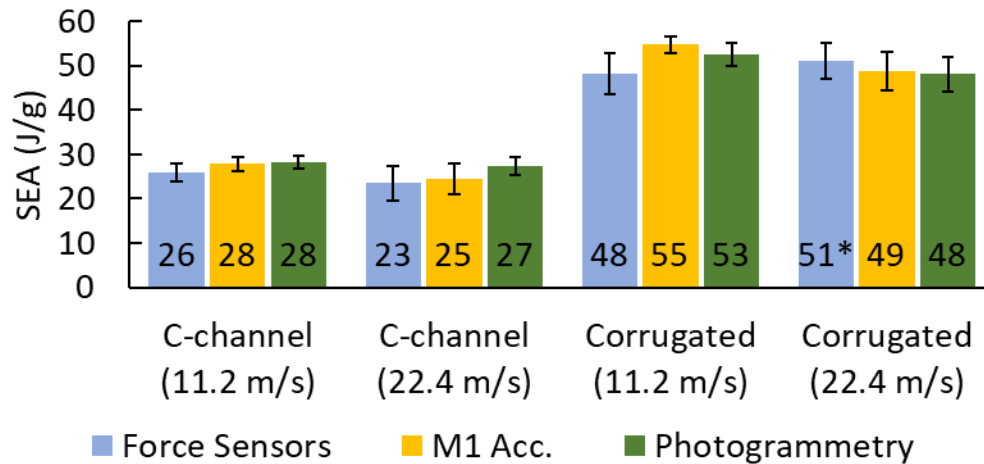

Figure 11. Summary of mean SEA results for the C-channel and corrugated specimens for both test conditions measured with transducers and photogrammetry. Error bars represent ±1 std. dev. *One of the force-sensor-measured SEAs was an outlier and removed from the dataset.

CONCLUSIONS & FUTURE WORK

A pneumatic-actuated crash sled was designed and built in the Ballistic Impact Laboratory at NASA Glenn Research Center. The sled was used to complete a test program to investigate effects of geometry and impact speed, keeping the impact kinetic energy approximately constant, on specific energy absorption (SEA) of triaxially-braided composite specimens. The results showed that the corrugated

specimens had approximately twice the SEA of the C-channel specimens. In addition, in the 11.2 to 22.4 m/s range of impact speeds used in this study, the speed had no significant effect on the SEA. This finding suggests that the SEA of triaxially braided T700S/TC275-1 carbon/epoxy is independent of the strain rates associated with the tested range of impact velocities.

There are several opportunities for future work based on the findings in this study. Digital image correlation should be used with the high-speed photogrammetry data to measure strain during the impact event and provide a better understanding of the failure modes. Length effects should be measured by testing specimens of varying lengths with the same cross section. In composite specimens, different resins and fiber architectures can be utilized to compare SEAs in various material systems. Interleaves, through-thickness stitching, and other interlaminar toughening techniques can be implemented to impede delamination. In addition, the support reaction can be varied to investigate changes in SEA and failure modes as a function of M_2.

ACKNOWLEDGEMENT

REFERENCES

Carruthers, J. J., Kettle, A. P., & Robinson, A. M. (1998). Energy Absorption Capability and Crashworthiness of Composite Material Structures: A Review. *Applied Mechanics Reviews*, *51*(10), 635-649.

Farley, G. L. (1986). Effect of Fiber and Matrix Maximum Strain on the Energy Absorption of Composite Materials. *Journal of Composite Materials*, *20*(4), 322-334.

Farley, G. L. (1989). Energy-Absorption Capability and Scalability of Square Cross Section Composite Tube Specimens. *Journal of the American Helicopter Society*, *34*(2), 59-62.

Farley, G. L. (1991). The Effects of Crushing Speed on the Energy-Absorption Capability of Composite Tubes. *Journal of Composite Materials*, *25*(10), 1314-1329.

Garner, D. M., and Adams, D. O. (2008). Test Methods for Composites Crashworthiness: A Review. *Journal of Advanced Materials*, *40*(4), 5-26.

Herrmann, H., Mohrdieck, C., and Bjekovic, R. (2002). Materials for the Automotive Lightweight Design. Presented at FKA/IKA Conferences New Advances in Body Engineering, Aachen, Germany, 17.

Jacob, G. C., Fellers, J. F., Simunovic, S., and Starbuck, J. M. (2002). Energy Absorption in Polymer Composites for Automotive Crashworthiness. *Journal of Composite Materials*, *36*(7), 813-850.

Zhou, W., Craig, J., and Hanagud, S. (1991). Crashworthy Behavior of Graphite/Epoxy Composite Sine Wave Webs. In Proceedings of the 32nd Structures, Structural Dynamics, and Materials Conference, AIAA, Baltimore, MD, 1618– 1626.